Supplementary Information

Reduced graphene oxide: Firm support for catalytically active palladium nanoparticles and game changer in selective hydrogenations

Manuela Cano[a], Ana M. Benito[a], Esteban P. Urriolabeitía[b], Raul Arenal[c,d] and Wolfgang K. Maser[*a]

[a]ICB-CSIC, E-50018 Zaragoza, Spain. [*]wmaser@icb.csic.es
[b]ISQCH-CSIC-Univ. Zaragoza, E-50009 Zaragoza, Spain
[c]LMA-INA-Univ. Zaragoza, E-50018 Zaragoza, Spain
[d]Fundacion ARAID, Zaragoza, E-50018 Zaragoza, Spain

S1. Experimental

S1.1 Materials

All reagents and solvents were obtained from Sigma-Aldrich Co., St. Louis, MO, USA).

S1.2 Preparation of graphite oxide, graphene oxide and reduced graphene oxide

(a) Graphite oxide was prepared, using a modified Hummers' method, from graphite powder by oxidation with $NaNO_3$, H_2SO_4 and $KMnO_4$ in an ice bath as reported in detail elsewhere;[1, 2] (b) A suspension of graphene oxide (GO) sheets was prepared as reported elsewhere.[3, 4] In brief, the prepared graphite oxide powder was sonicated in distilled water (1 mg/mL) for 2 hours, followed by mild centrifugation of the suspension at 4500 rpm for 60 min. The separated brown-coloured supernatant water GO dispersion had a concentration of 0.35 mg/mL. (c) Reduced graphene oxide (RGO) was prepared by adding an excess of hydrazine hydrate $N_2H_4 \cdot H_2O$ (900 μL) to the GO dispersion and stirred under reflux for 5 hours. Filtration through a polycarbonate membrane filter of 3 μm pore size, followed by washing with 200 mL of distilled water and vacuum drying at 80 °C for 48 afforded the powder-like RGO material.

S1.3 Preparation of palladium precursor dilithiumtetrachloropalladate(II) $Li_2[PdCl_4]$

$PdCl_2$ (23 mg, 0.13mmol) was suspended in water (5 mL). LiCl was added in excess (27 mg), 0.5 mmol). The resulting mixture was refluxed for 1 hour until complete dissolution of the palladium salt, affording a clear deep-red $Li_2[PdCl_4]$ solution (34 mg, 0.13 mmol)

S1.4 Preparation of Pd-NP/RGO hybrid material using $Li_2[PdCl_4]$ precursor

GO was reacted with $Li_2[PdCl_4]$ in a 1:1 weight percent ratio as follows: 100 mL of the prepared GO solution (containing 35 mg of GO) was added to the prepared $Li_2[PdCl_4]$ solution (containing 35 mg of the complex). The resulting $Li_2[PdCl_4]$/GO mixture was reflux heated under stirring for 1.5 hours. Subsequently, an excess of hydrazine hydrate $N_2H_4{\cdot}H_2O$ (900 µL) was added to the hot suspension. Stirring under reflux continued for an additional 5 hours before the suspension was allowed to cool down to room temperature. Filtration through a polycarbonate membrane filter of 3 µm pore size, followed by washing with 200 mL of distilled water and vacuum drying at 80 ˚C for 48 afforded the powder-like Pd-NP/RGO material containing 34 wt.% of Pd. This material was used for further characterization and subsequent hydrogenation reactions. In the same way, “low-loading” catalysts were prepared using GO : $Li_2[PdCl_4]$ weight ratios of 10:1 and 20:1. The resulting Pd-NP/RGO hybrid materials contained 12.6 wt.% and 2.6 wt.% of Pd, respectively.

S1.5 Preparation of Pd-NPs/RGO hybrid material using [$Pd_2(dba)_3CHCl_3$]precursor

In previous communications[5, 6] we reported that the reaction of MWCNTs with the palladium complex [$Pd_2(dba)_3 \cdot CHCl_3$] (dba = dibenzylideneacetone) using reflux or microwave techniques afforded the hybrid material Pd-NPs/MWCNTs with high loading of Pd (up to 40 wt.%) in reaction times ranging from 2 h (reflux) to few minutes (microwaves). In an analogous way we reacted here RGO and [$Pd_2(dba)_3 \cdot CHCl_3$] in a 1:1 ratio in dry toluene at 110 ºC affording Pd-NP/RGO hybrid material with a Pd load of only 5 wt.% for both, reflux and microwave heating process. With an efficiency of below 30%, this synthesis method was not considered any longer of practical interest for the preparation of Pd-NP/RGO materials employed in hydrogenation applications.

S1.6 Catalytic hydrogenation experiments

Hydrogenation experiments were carried out exclusively with the “high-loading” Pd-NP/RGO material containing 34 wt.% of Pd (please note: Since high- and low-loading hybrid materials are equally composed of small-sized nanoparticles (see below in S2) it is preferred to use the hybrid material with the maximum Pd loading thus avoiding the use of larger amounts of the overall hybrid material for the hydrogenation reactions). To this end, the palladium catalyst supported on RGO in the appropriate amount (see article Table 1), was dispersed in $CHCl_3$ (2 mL) under stirring in a 5 mL round-bottomed flask at room temperature and atmospheric pressure. To this suspension 1 mmol of the substrate to be hydrogenated was added. The system was then evacuated and backfilled with H_2 in cycles for at least five times. The pressure of H_2 was kept constant (p_{H2} = 1 atm) with a balloon system during the whole reaction time. Once the hydrogenation has been performed, the resulting suspension was filtered through a 3 µm pore polycarbonate membrane filter, and the solid catalyst material was washed with CH_2Cl_2 and water, and dried at 110 °C overnight. The solvent was removed from the organic solution by fractional distillation, affording the hydrogenated products as oily residues, which were characterized by ^1H and ^{13}C NMR spectroscopy and the spectral data were compared with data from corresponding reference samples found in the literature data bases. Recyclability tests were performed for the case of 1,3,5-cycloheptatriene using 2.5% of Pd in the Pd-NP/RGO catalyst system and a hydrogenation time of 5h. Four consecutive reactions were carried out. After each run the catalyst was isolated by filtration, washed and dried before a new batch of reactant is added. Activity (product yield), selectivity (production conversion) were analyzed after each run by NMR technique as explained above. The amount of palladium retained was determined by ICPS after the final run.

S1.7. Characterization of the hybrid materials and hydrogenation products

The morphology of the prepared hybrid materials was studied by transmission electron microscopy (TEM, JEOL-2000 FXII working at 200 kV and a high-resolution Cs-corrected Titan-Cube microscope working at 80 kV). Samples were dispersed in ethanol in ultrasound bath for 10 min, and a drop of the suspension was placed onto a copper grid coated with carbon film. Powder X-ray diffraction (XRD) measurements were carried out at room temperature on a Bruker D8 Advance diffractometer using a Cu Kα X-ray radiation. Peak position and indexing was performed using Bruker TOPAS and EVA software packets. The metal loading in the carbonaceous samples was determined by Inductive coupled plasma spectroscopy (ICPS) using a Jobin-Yvon 2000 Ultrace Analyzer. X-ray photoelectron spectroscopy (XPS) was carried out on an ESCAPlus

Omicron spectrometer using a monochromatized Mg X-ray source (1253.6 eV). Data were analyzed using CasaXPS software packet. Raman spectra were recorded with a Horiba Jobin Yvon HR800 UV spectrometer using an excitation wavelength of 532 nm. BET specific surface area was calculated from nitrogen adsorption isotherms acquired at liquid nitrogen temperature on a Micromeritics ASAP 2010 adsorption apparatus. ^{1}H and ^{13}C NMR spectra of the hydrogenation products were taken in CD_2Cl_2, $CDCl_3$ or acetone-d_6 solutions at 25 °C on Bruker Avance-300 and Avance-400 spectrometers (δ, ppm; J, Hz), and referenced using the solvent signal as internal standard.

S2. Results

S2.1 TEM results for Pd-NP/RGO using $Li_2[PdCl_4]$ precursor

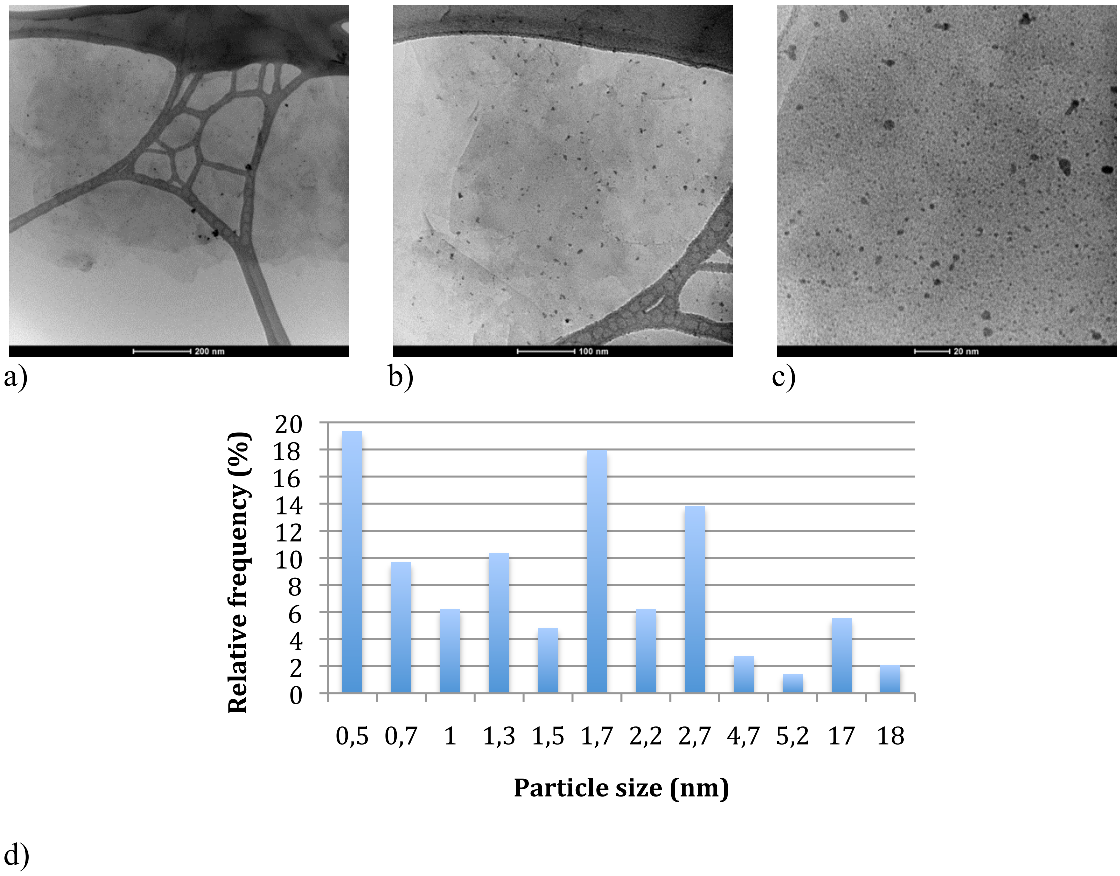

Figure S2.1. TEM images of hybrid materials synthesized from precursor $Li_2[PdCl_4]$ at three different areas and scales (a-c) and particle size distribution (d).

Figures S1 (a-c) shows TEM images of hybrid materials synthesized from precursor $Li_2[PdCl_4]$ at different scales. At highest magnification (c) a uniform distribution of small-sized nanoparticles in the range of 0.5 to 5 nm can be seen. These are accompanied by a significantly lower number of some larger-sized nanoparticles in the range of 18 nm. Very similar distributions can be seen in other areas (a,b). The larger magnification only should point out the rather homogeneous coverage of the RGO sheets. A typical particle size distribution is depicted in (d) obtained from evaluation of 145 particles on figure (c). Average particle size is about 3 to 4 nm. The presence of functional groups on the initial GO sheets may either favor the attachement (electrostatic or covalent) of Pd nanoparticles or/and affect their mobility on an otherwise smooth surface, thus efficiently reducing the possibility for clustering into larger nanoparticles,[7, 8] as observed when using RGO sheets and metal complexes with Pd in the neutral state (see S2.2).

S2.2 TEM results for "low-loading" Pd-NP/RGO hybrids using $Li_2[PdCl_4]$ precursor

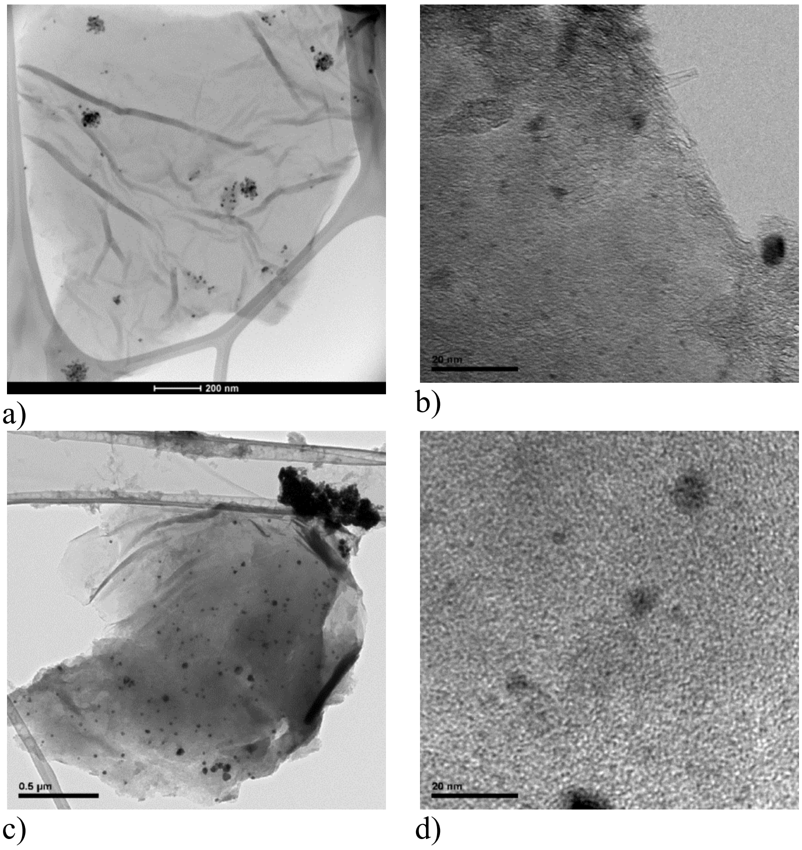

Figure S2.2. TEM images of hybrid materials synthesized form precursor $Li_2[PdCl_4]$. (a) and (b) GO: $Li_2[PdCl_4]$ 10:1 weight ratio at low and high magnification, respectively. (c) and (d) GO:$Li_2[PdCl_4]$ 20:1 weight ratio at low and high magnification, respectively.

TEM images of the "low-loading" Pd-NP/RGO hybrid materials (Figure S2.2) do not reveal esssential differences compared to the high-loading sample (Figure S1). At high magnification scales (Figure S2.2 b,d) Pd nanopatices of sizes below 10 nm easily can be spotted throughout different areas of the sample. In addition, larger isolated Pd nanoparticles beyond 10 nm or even complete areas of larger Pd agglomerates can be observed at lower magnification (Figure S2.2 a,c). In this sense it is worthwhile to take into account the following consideration: While TEM, as a highly local technique, is of special value for the detection of small sized nanoparticles and their distribution no reliable information can be obtained concerning larger agglomerates of Pd nanoparticles, their sizes and their spatial distribution.

S2.3. XRD results for Pd-NP/RGO using $Li_2[PdCl_4]$ precursor

X-ray diffraction (XRD) as a bulk technique providing information on diffracting crystallite planes covers all different crystallite size domains. Applying the Debye-Scherrer equation, the average crystallite sizes can be determined from the FWHM of the diffraction peaks.[9] This is suitable for crystallite sizes in the range from 100 nm down to 10 nm. Below this value it is not applicable anymore. Providing selectively information on crystallite sizes above 10 nm XRD thus is a suitable technique to reveal the existence of larger agglomerated nanopaticles in the prepared Pd-NPs/RGO hybrid materials (while no information can be extracted on particle sizes below 10 nm).

Figure S2.3 shows the X-Ray powder diffractograms of the Pd-NP/RGO hybrid materials. For all the prepared concentrations, the diffraction peaks of Pd^0 can be clearly observed. The crystallite sizes applying the Debye-Scherrer equation are summarized in Table S2.1.

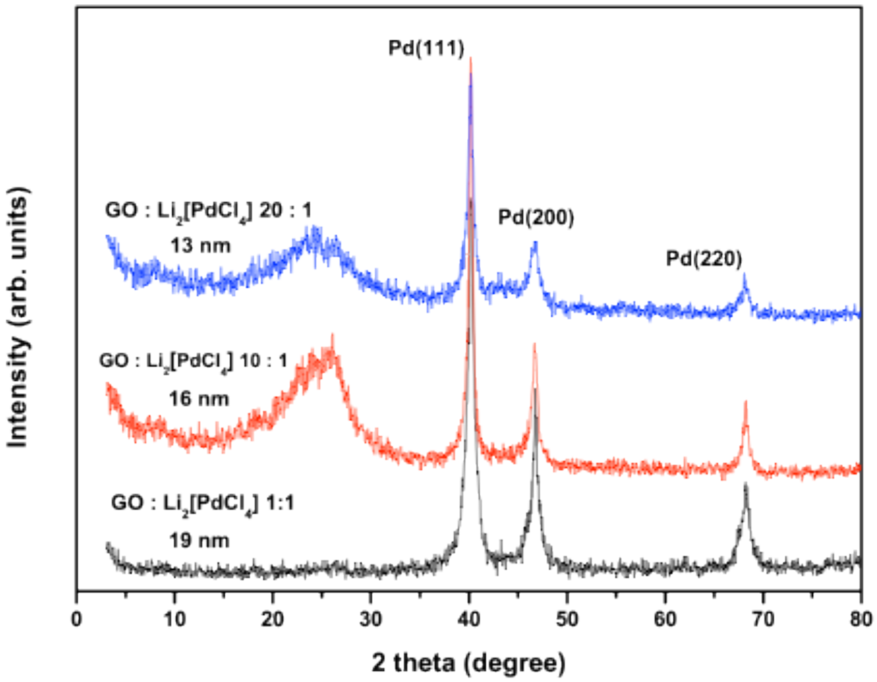

Figure S2.3. X-ray powder diffractograms of Pd-NP/RGO hybrids of different concentrations. Concentration and average crystallite size from Debye-Scherrer analysis are indicated.

Table S2.1. Crystallite size of Pd in the Pd-NP/RGO hybrid materials with different Pd loadings

GO : $Li_2[PdCl_4]$ weight ratio$^+$	Pd loading (wt.%)$^{++}$	Crystallite size (nm)$^{+++}$
1 : 1	34	19
10 : 1	12.5	16
20 : 1	2.5	11

$^+$used in synthesis. $^{++}$determined by ICPS. $^{+++}$determined by Debye-Scherrer formula

As can be seen from Table S2.1, the higher the Pd loading in the final hybrid material so larger the Pd crystallite size, and correspondingly the size of the individual Pd nanoparticles. The picture which emerges from XRD and TEM observations is the following: Pd nanoparticles of sizes in between 2 to 10 nm with average size of about 4 nm are obtained independently of the used Pd concentration. This again may underline important role of oxygen funtional groups of the starting GO material serving as nucleation points. Additionally at higher Pd concentrations larger Pd nanoparticles seem to form more likely.

S2.4. Mechanism for the formation of large-sized Pd nanoparticles

Two principal scenarios could be envisaged:

(a) Pd nanoparticles well-anchored by the functional oxygen groups of the initial GO support serve as nucleation points for continuous growth favored by enhanced Pd precursor concentrations. However, the experimental facts do not fully support this mechanism.

(b) Pd precursors which do not directly “find” functional oxygen group on the GO support maintain their high mobility and thus easily can form larger-sized nanoparticles before being trapped at a suitable defect site where there even can build-up larger agglomerates covering wider areas of the R(GO) support. This process will be favored by higher precursor concentrations. However, it also explains the formation of agglomerates at low Pd precursor concentrations, as for example seen in the upper right corner of Figure S2.2 (c). Thus this mechanism seems to provide a somewhat more likely explanation for the experimental facts.

Summarizing: Small sized nanoparticles with average size of 4 nm are formed due the interaction with functional oxygen groups on the initial GO support. This is independent of the used precursor amount. However, larger-sized nanoparticles or agglomerates, which additionally can be observed, originate from Pd nanoparticles which are not anchored on free-oxygen groups. This type of initial Pd nanoparticles are highly mobile and prone to create larger particles before trapped at a defect site where eventually they can form agglomerates covering even wider zones of the GO support. The formation of these larger nanoparticles indeed is favored by higher amounts of initial Pd precursor amounts. However, at the same time the possibility of forming larger-sized nanoparticles and agglomerates strongly depends as well on the “quality” of the initial

GO support material, i.e. the number/density of functional oxygen groups and topological defects. The lower the number/density of functional oxygen groups and topological defects, so more likely is the formation of larger nanoparticles and agglomerates. This is as can be seen by in the following section S2.5, where RGO was used as starting support material.

S2.5. TEM results of Pd-NP/RGO from $Pd_2(dba)_3CHCl_3$ precursor

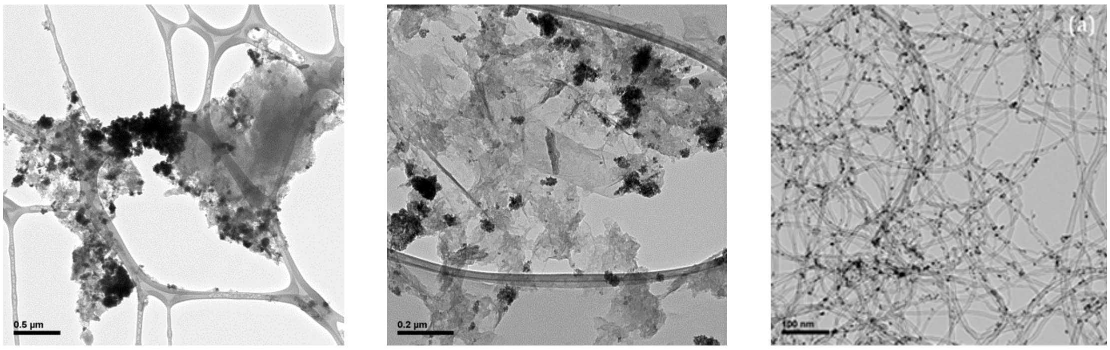

a) b) c)

Figure S2.4 TEM images of hybrid materials synthesized from precursor $Pd_2(dba)_3CHCl_3$ in toluene: (a, b) Pd-NPs/RGO and (c) Pd-NPs/MWCNTs.

Figure S2 shows TEM images of hybrid materials synthesized form precursor $Pd_2(dba)_3CHCl_3$ in toluene using the route described in S1.4. In contrast to the Pd-NPs/RGO material prepared from the $Li_2[PdCl_4]$ precursor larger Pd tends to form larger agglomerates about 20 nm not uniformly distributed on the RGO sheets, which also seem to have a more degenerated aspect. However, the initial starting conditions of the two methods are not comparable and there is space for improvement. Especially in light of results obtained using this precursor for MWCNTs and resulting Pd-NP/MWCNT composites. Here a homogeneous distribution of Pd-NPs with sizes of 4 nm well-supported on CNTs was obtained (Figure S1 c). Although functional groups are absent in the used MWCNTs, curvature and other topological defects may contribute to a reduced mobility of Pd-NPs thus contributing to avoid clustering. On the other hand, the results obtained for RGO may point out that this precursor route either is not yet fully adapted to obtain nanoparticles of small diameter firmly attached to RGO or, due to a lower degree of topological surface defects, is inherently prone to forming larger clusters of nanoparticles on its surface.

S2.6 XRD results of Pd-NP/RGO from $Pd_2(dba)_3CHCl_3$ precursor

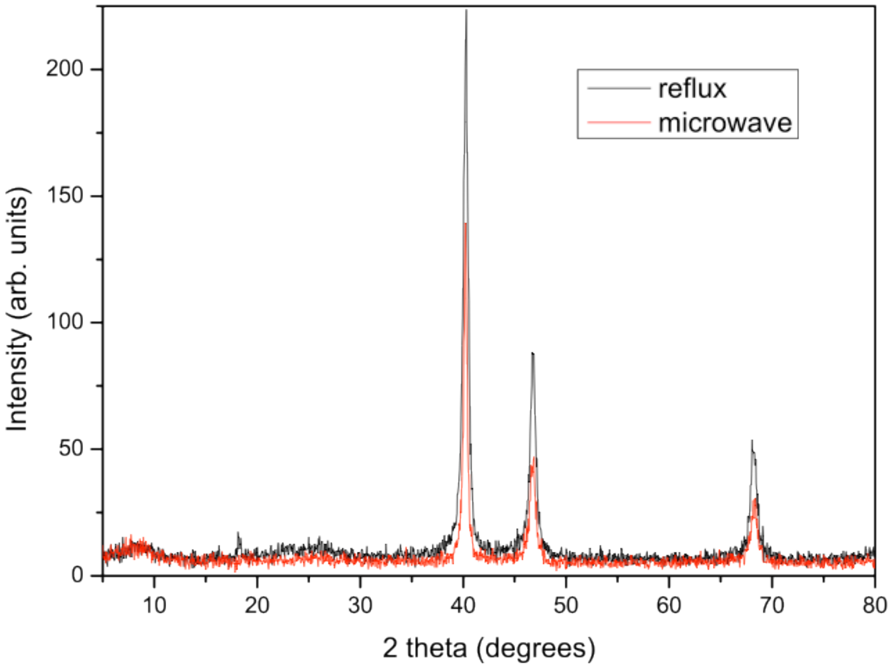

Figure S3. X-ray diffractograms of Pd-NPs/RGO material prepared from $Pd_2(dba)_3CHCl_3$ precursor under reflux and short time microwave process.

The three dominant peeks in Figure S3 at about 40 °, 47 ° and 68 ° correspond to the (111), (200) and (220) Bragg reflections of face-centred cubic Pd. In contrast to the Pd-NPs/RGO material prepared from $Li_2[PdCl_4]$ precursor, the peaks are of much higher intensity with respect to the underlying RGO background (indicated by the weak and broad peak at about 25 °). Furthermore the smaller FWHM indicates larger crystallite sizes, probably related to the formation of larger Pd clusters, as also seen in TEM (see Figure S.1).

S2.7 Specific surface area of the Pd-NP/RGO hybrid material

Specific surface area of the catalyst was determined from nitrogen adsorption isotherms (BET) measurements for the RGO support material.

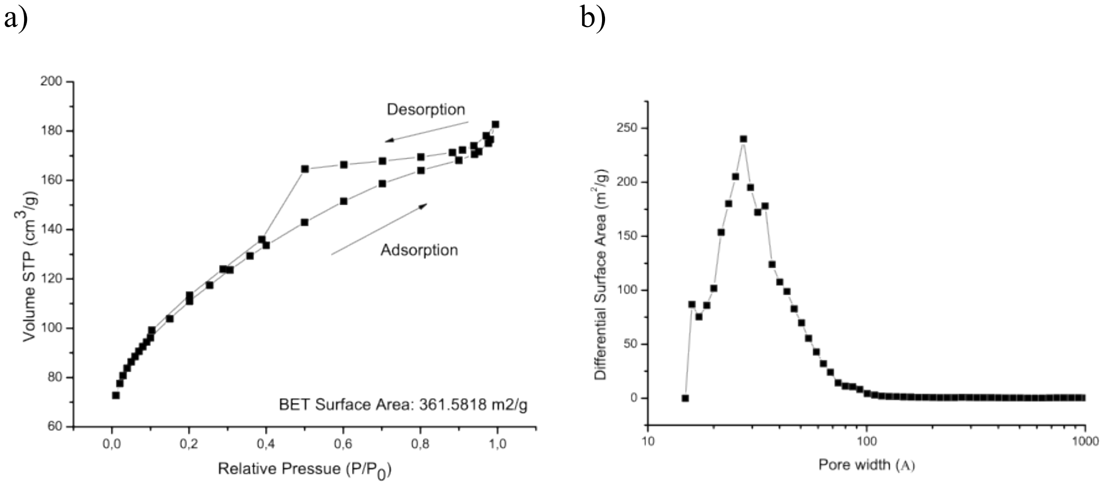

Figure S4. (a) Nitrogen adsorption isotherms of RGO support material. (b) Differential surface area as a function of pore width.

The nitrogen adsorption isotherm of the RGO support material in Figure 4a reveals a BET surface area of 361 m^2/g. Being of Type 4 it indicates the presence of micro and mesopores. The resulting pore size distribution shown in Figure 4b clearly reveals the dominance of small sized mesopores with a maximum at about 3 nm. These results are in-line with values reported in literature[10], but still below the theoretical value of 1700 m^2/g for isolated RGO sheets.[11] due to agglomerations and partial overlapping of reduced sheets.[10]

Taking into account the experimentally determined BET surface area of RGO, the average Pd-NPs diameter as determined by TEM, and the mass of Pd and RGO of the overall catalyst system the specific surface area of the overall Pd-NPs/RGO catalyst system of 315 m^2/g was obtained. The corresponding calculations and resulting values are summarized in Table S1 (please note that the synthesized quantities of the overall catalyst material were not sufficient for carrying out reliable BET measurements on the Pd-NPs/RGO material itself). In addition to the values based on the experimental BET results for RGO shown in the second column of Table S1, for the sake of comparison, the last column provides values based on the surface area for an ideal sheet of RGO of 1700 m^2/g.[11]

Table S1. Estimation of specific surface area (SSA) of the Pd-NPs/RGO hybrid

Specific surface area (SSA) of RGO (m^2/g)	360	1700[+++]
Mass of RGO (g)	35	35
Surface area of 35 mg RGO (m^2)	12.5	59.5
Average diameter of Pd NPs (nm) according to TEM analysis	4	4
Average surface area of Pd NPs (nm^2)	50	50
Average catalytically active surface area of Pd NPs (nm^2)[+]	40	40
Total number of isolated Pd NPs covering surface area of 35 mg GO (m^2)	3 x 10^9	6 x 10^9
Surface area of total number of isolated Pd NPs (m^2)	1.5x 10^{-7}	3 x 10^{-7}
Mass of Pd-NPs/RGO hybrid (mg)	40	40
SSA of Pd-NPs/RGO hybrid (m^2/g)[++]	315	1490
Difference SSA hybrid and GO (m^2/g)	45	210
Percentage of SSA difference (%)	12.5	12.5

[+] Value taking into account that only 80% of Pd are in catalytically active Pd^0 state (according to XPS results).

[++] SSA_{hybrid} = (surface $area_{RGO}$ – surface $area_{Pd}$)/$mass_{hybrid}$.

[+++] last column corresponds to calculations for an ideal surface area of a single RGO sheet of 1700 m^2/g.[11]

References

1. W. S. Hummers and R. E. Offeman, *Journal of the American Chemical Society*, 1958, **80**, 1339.
2. X. L. Li, G. Y. Zhang, X. D. Bai, X. M. Sun, X. R. Wang, E. Wang and H. J. Dai, *Nat. Nanotechnol.*, 2008, **3**, 538-542.
3. C. Vallés, P. Jiménez, E. Muñoz, A. M. Benito and W. K. Maser, *The Journal of Physical Chemistry C*, 2011, **115**, 10468-10474.
4. C. Vallés, J. D. Núñez, A. M. Benito and W. K. Maser, *Carbon*, 2011, **50**, 835-844.
5. M. Cano, A. M. Benito, W. K. Maser and E. P. Urriolabeitia, *Carbon*, 2011, **49**, 652-658.
6. M. Cano, A. M. Benito, W. K. Maser and E. P. Urriolabeitia, *New Journal of Chemistry*, 2013, **37**, 1968-1972.
7. C. Nethravathi, E. A. Anumol, M. Rajamathi and N. Ravishankar, *Nanoscale*, 2011, **3**, 569-571.
8. J. A. Rodríguez-Manzo, O. Cretu and F. Banhart, *ACS Nano*, 2010, **4**, 3422-3428.
9. B. E. Warren, *X-ray diffraction*, Dover Publications, Inc., New York, 1969.
10. S. Stankovich, D. A. Dikin, R. D. Piner, K. A. Kohlhaas, A. Kleinhammes, Y. Jia, Y. Wu, S. T. Nguyen and R. S. Ruoff, *Carbon*, 2007, **45**, 1558-1565.
11. T. Szabó, E. Tombácz, E. Illés and I. Dékány, *Carbon*, 2006, **44**, 537-545.